Tunable Third-Order Nonlinear Optical Response in ϵ-Near-Zero Multilayer Metamaterials

Domenico Genchi◉, Ionut Gabriel Balasa◉, Tiziana Cesca◉,* and Giovanni Mattei◉

Department of Physics and Astronomy, NanoStructures Group (NSG), University of Padua, via Marzolo 8, Padova I-35131, Italy

Metamaterials with properly engineered linear and nonlinear optical response are of great interest for many advanced applications in nanophotonics and quantum optics. In the present work, we perform a detailed spectral investigation of the third-order nonlinear optical properties (nonlinear refractive index and nonlinear absorption coefficient) of ϵ-near-zero Au/Al$_2$O$_3$ multilayer metamaterials in a broad range of the visible spectrum across their ϵ-near-zero (ENZ) wavelength, at different incidence angles with TE- and TM-polarized light. Multilayers with different gold filling fractions (16 and 33%) are produced by magnetron sputtering to tune the spectral position of the ϵ-near-zero wavelength. The results demonstrate that a continuous modulation of the linear and nonlinear optical parameters of these metamaterials can be obtained as a function of the angle of incidence, with a peak of the nonlinear optical coefficients close to the ENZ wavelength. A model is proposed to describe the nonlinear optical response of the metamaterials, and an optimal agreement between experimental and simulated results is obtained in all the configurations explored. This model represents a useful tool to design multilayer metamaterials with tailored nonlinear optical properties, to be used in different experimental configurations.

I. INTRODUCTION

Optical metamaterials (MMs)—composite materials artificially structured on a subwavelength scale—have been the object of intense research in the past few years for the possibility to obtain unconventional functionalities, which are not accessible by the material constituents and can be engineered by properly designing the metamaterial structure [1–3]. The capability to tailor the linear and nonlinear optical response of plasmonic metamaterials is of great interest for many advanced applications in nanophotonics and quantum optics, and different geometries have been proposed [4–9]. Beside this, the availability of actively tunable metamaterials, whose optical response can be controlled by acting on some external parameters, has further broadened their field of applications [10–12].

More recently, much attention has been gained by a peculiar class of metal-dielectric metamaterials, namely ϵ-near-zero (ENZ) metamaterials [13,14]. These are anisotropic uniaxial metamaterials, arranged as metal-dielectric stacks or metal nanowires embedded in a dielectric matrix, in which the real part of one of the diagonal components of the effective permittivity tensor changes sign as a function of the wavelength, vanishing at the so-called ENZ wavelength. In correspondence of this, the metamaterial undergoes an optical topological transition as its dispersion law for extraordinary (transverse magnetic)

waves changes from elliptic to hyperbolic [15]. Intriguing phenomena and applications have been demonstrated for these metamaterials in the hyperbolic regime and close to the ENZ wavelength [14–19], among which an amplified Kerr-type nonlinear optical response has been recently reported [9,20].

In the present work, we perform a broadband spectral characterization in the visible range of the linear and third-order nonlinear optical properties of gold-alumina multilayer metamaterials at different angles of incidence for TE and TM polarization, across their ENZ wavelength. A continuous modulation of the nonlinear optical coefficients (nonlinear refractive index and nonlinear absorption coefficient) is obtained by changing the incident angle demonstrating that, for this class of metamaterials, tilting the samples is a simple and effective method to get a fine tuning of their nonlinear response. Moreover, we propose a model to simulate the nonlinear optical parameters of the metamaterials in the different investigated configurations, which represents a useful predictive tool to design multilayer metamaterials with tailored and tunable nonlinear optical response.

II. RESULTS AND DISCUSSION

A. Linear optical properties

The investigated multilayer metamaterials are composed of alternating layers of Au and Al$_2$O$_3$ arranged in a four-period structure on soda-lime glass substrates, in order to
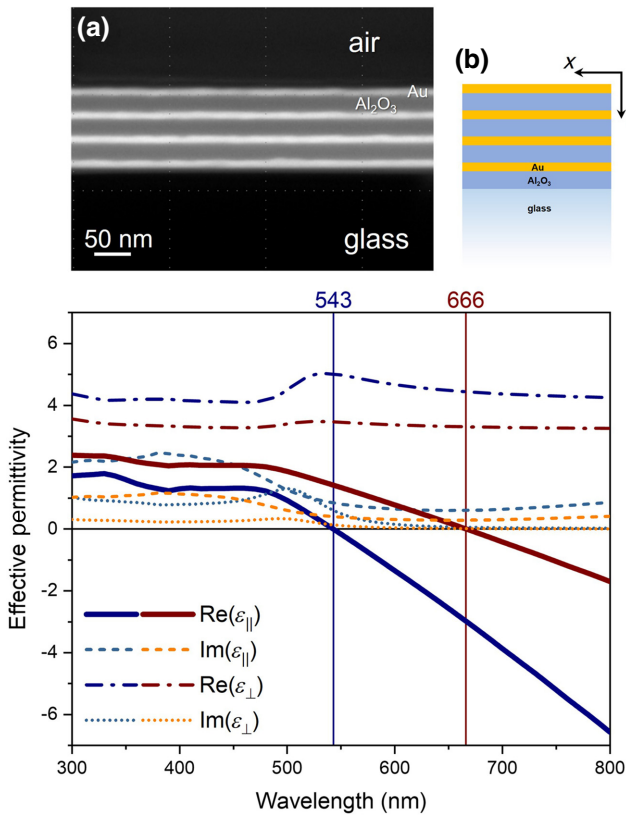
---

*tiziana.cesca@unipd.it

FIG. 1.   (a) Cross-section SEM image of the MM33 Au/Al$_2$O$_3$ multilayer metamaterial (metal filling fraction $f_m = 33\%$). (b) Sketch of the multilayers used for the numerical simulations. (c) Effective permittivity of samples MM16 (red) and MM33 (blue). For both samples, the real (solid, dash-dot) and imaginary (dash, dot) parts of the in-plane $\epsilon_\parallel$ and out-of-plane $\epsilon_\perp$ components are, respectively, depicted. The vertical solid lines indicate the λ_{ENZ} of each MM.

obtain a different metal filling fraction: $f_m = 33\%$ (sample MM33) and $f_m = 16\%$ (sample MM16). As an example, Fig. 1(a) shows the cross-section SEM image of sample MM33. A sketch of the sample structure used for the numerical simulations is reported in Fig. 1(b). The SEM image of sample MM16 and the results of topographical characterizations performed by AFM on both MMs are reported in Fig. S1 of the Supplemental Material [21].

The *in-plane* ($\epsilon_\parallel = \epsilon_x = \epsilon_y$) and *out-of-plane* ($\epsilon_\perp = \epsilon_z$) complex effective permittivities of the multilayer MMs are calculated within the effective medium theory (EMT) [22,23] using Eqs. (10) and (11) (see Sec. IV). The results for both samples, MM33 and MM16, are reported in Fig. 1(c). The vertical solid lines indicate the ϵ-near-zero wavelength, i.e., the zero-crossing point of the real part of $\epsilon_\parallel$, corresponding to the transition condition of the metamaterial optical response from the elliptic regime [Re($\epsilon_\parallel$) > 0, Re($\epsilon_\perp$) > 0] to the hyperbolic one [Re($\epsilon_\parallel$) < 0, Re($\epsilon_\perp$) > 0]

[15,22,24,25]. A significant redshift of the ENZ spectral position is obtained by increasing the thickness of the dielectric layers, that is by decreasing the metal filling fraction [13]. In the case of the studied gold-alumina multilayers, it results $\lambda_{ENZ} = 666$ nm for MM16 and $\lambda_{ENZ} = 543$ nm for MM33, i.e., by keeping a metal thickness of 15 nm a shift of λ_{ENZ} by more than 120 nm is obtained with a variation of 50 nm in the dielectric thickness. Moreover, the increase of dielectric thickness gives rise to a reduction of the MM losses owing to smaller imaginary components [see Fig. 1(c)]. More generally, in Fig. S2 of the Supplemental Material [21] we report the real and imaginary components of the in-plane and out-of-plane effective permittivities, and the ENZ wavelength, of Au/Al$_2$O$_3$ multilayers, calculated within the effective medium approximation (EMA) as a function of the metal filling fraction, which demonstrate the possibility to finely tune the dielectric properties of the multilayer metamaterials in the visible range by simply controlling the dielectric thickness.

The capability to engineer the dielectric properties of metamaterials by changing the fabrication parameters allows us to control their linear optical response. Besides, further degrees of freedom can be used, such as the angle of incidence and the polarization (TE or TM) of the light beam impinging on them. In Fig. 2 we report the spectra of reflectance (R), transmittance (T), and absorptance (A) of MM16 (left panels) and MM33 (right panels) as a function of the incidence angle and the light polarization. The experimental data (open symbols) are measured with a spectroscopic ellipsometer and are compared with the numerical simulations (solid curves) performed by EMUstack (see Sec. IV) [26]. The experimental absorptance data are calculated as $A = 1 - R - T$ starting from the experimental data of R and T. At normal incidence (black), the experimental reflectance could not be measured, so we report the experimental transmittance values only. On the whole, the simulated curves fit very well the experimental data for all the analyzed conditions and the small discrepancies are very likely generated by little differences of thickness or morphological imperfections in the produced samples with respect to the implemented models, which conversely are ideal defectless metal-dielectric stacks. For the MM16 sample, at normal incidence (black) the reflectance spectrum shows an abrupt change around λ_{ENZ}. For $\lambda > \lambda_{ENZ}$ the reflectance quickly increases tending to unity due to a growing metallic character of the metamaterial [22]. Conversely, at $\lambda < \lambda_{ENZ}$ lower values of R are observed. Moreover, oscillations appear in the R, T, and A spectra due to bulk plasmon polaritons (BPPs), which are generated by the constructive interference (spatial mode matching) between the surface plasmon polaritons (SPPs) sustained by the metal-dielectric interfaces of the MM, and they are extremely confined in the alumina layers sandwiched between two gold ones [10,18,27].
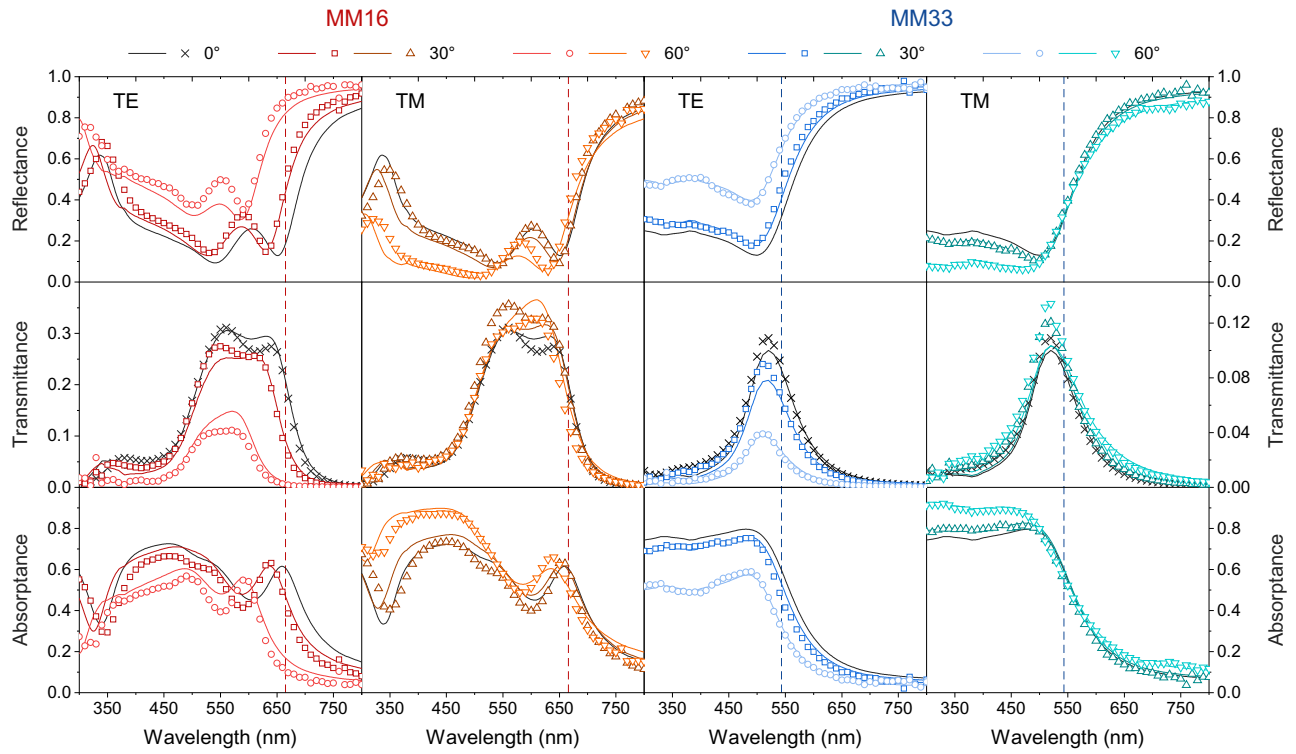
FIG. 2.   Reflectance (R), transmittance (T) and absorptance ($A = 1 - R - T$) spectra of the samples MM16 (left panels, left-hand scales) and MM33 (right panels, right-hand scales) at different angles of incidence ($0°$, $30°$, and $60°$) for TE and TM polarization. The experimental data (open symbols) are compared to the simulated curves (solid lines). The vertical dashed lines indicate the λ_{ENZ} of each sample: $\lambda_{ENZ} = 666$ nm for MM16 and $\lambda_{ENZ} = 543$ nm for MM33. At normal incidence (black), reflectance could not be measured and only the experimental transmittance data are reported.

This plasmonic subwavelength confinement makes each metal-insulator-metal sandwich in the MM act as resonant cavities where the electric field is enhanced, thus generating an absorptance peak and a corresponding reflectance dip near the ENZ wavelength (666 nm), accompanied by a high transmittance window [18]. This ENZ resonance effect [28,29] is strictly related to the wavelength of permittivity zeroing where the field is largely enhanced and it is highlighted in Figs. 3(a) and 3(b), where we report the profile of the squared modulus of the electric field ($|E|^2$) propagating inside the sample, obtained by EMUstack simulations at λ_{ENZ} for different angles of incidence ($0°$, $30°$, $60°$) for TE and TM polarization. A significant variation of all the features is observed by changing the incidence angle and the polarization of the incoming light. With TE-polarized light R increases and blueshifts by increasing the incidence angle; with TM polarization the sample exhibits a similar blueshift of the reflectance spectra with increasing angle but R conversely decreases [24]. On the other hand, with TE-polarized light, the transmittance of the sample significantly decreases with increasing angle of incidence and its spectral shape is progressively modified. In particular, at an angle of $60°$ the double-peak feature is damped and becomes more similar to a wide band with a maximum

at 570 nm. Conversely, with TM-polarized light only slight differences of the transmittance curve are observed at $30°$ and $60°$ with a small increase of the values at the peaks. The spectral modifications of the features observed in the reflectance and transmittance spectra as a function of the incidence angle and light polarization reflect on the absorptance spectra of the sample. This is rather evident with TE-polarized light, indeed the absorptance peak appearing near λ_{ENZ} blueshifts by increasing the incidence angle, up to a shift of 70 nm at $60°$; moreover, a decrease of absorptance occurs at $60°$ with respect to normal incidence.

By contrast, with TM-polarized light only a slight blueshift of the A peak (20 nm at $60°$) and an increase in the interband region 350–550 nm are observed. The MM33 sample (right panels in Fig. 2) exhibits a different behavior with respect to the MM16 one, even though some similarities can be found when we consider its response as a function of the incidence angle and light polarization. First of all, at λ_{ENZ} (vertical dashed line) the linear optical properties of the metamaterial utterly change as a consequence of its transition from the elliptic to the hyperbolic regime. Independently of the incidence angle and light polarization, at λ_{ENZ} there is a steep increase of the sample reflectance, which saturates very close to unity at
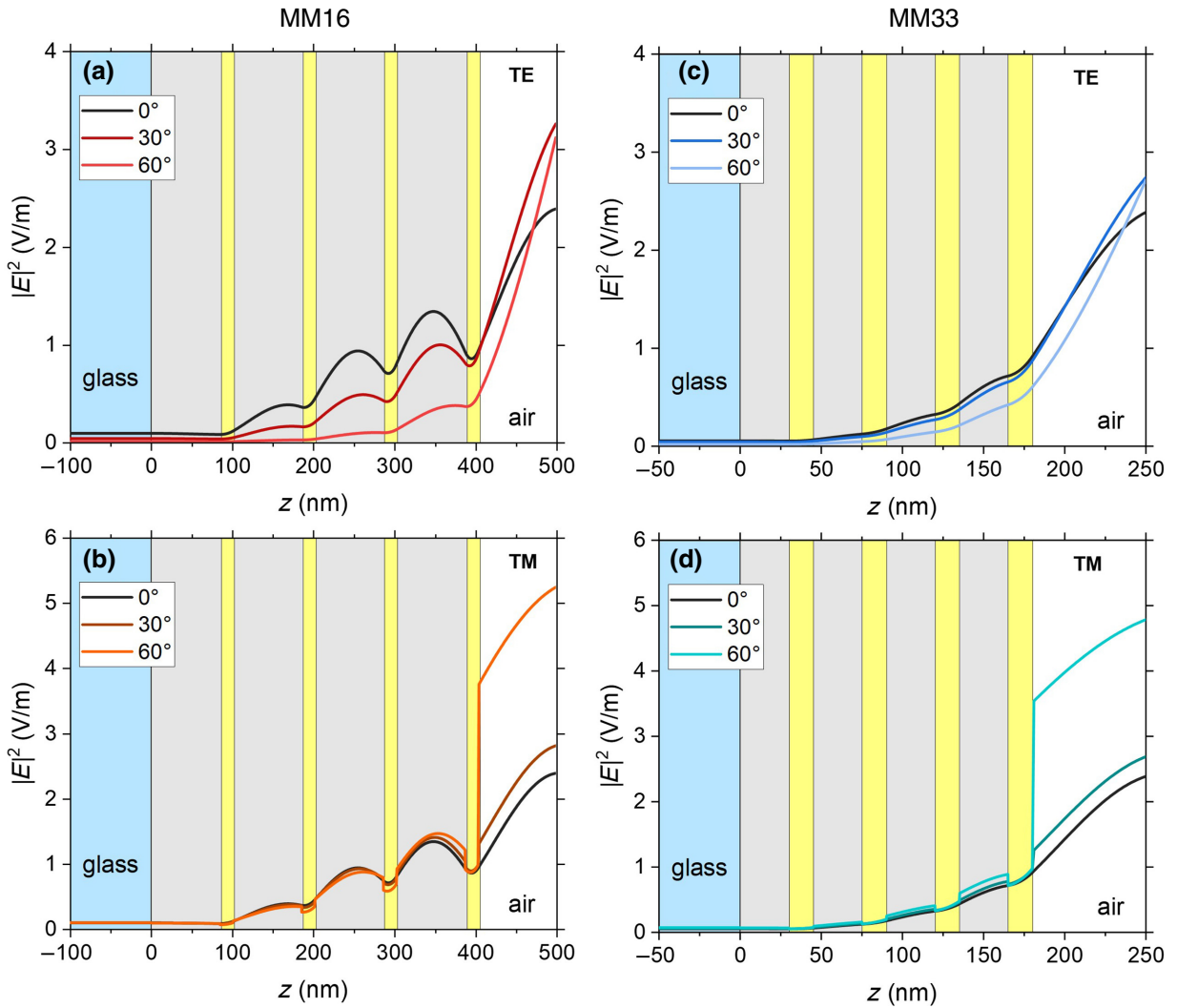
FIG. 3.   Depth profiles of $|E|^2$ inside the MM16 (a) and (b) and MM33 (c) and (d) samples, simulated by EMUstack at the corresponding λ_{ENZ} wavelength (666 nm for MM16 and 543 nm for MM33) for the different incidence angles indicated and for TE (a) and (c) and TM (b) and (d) polarization. A sketch of the multilayer structure used for the simulations is also superimposed to the curves. The beam is impinging normally to the samples from the air side, with an amplitude of 1 V/m. The incidence half-space (air) contains both the input beam and the reflected one.

$\lambda > \lambda_{ENZ}$ [22]. In the same way, its transmittance and its absorptance rapidly drop to a value very close to zero in the hyperbolic regime. Differently from MM16, no oscillations in the spectra are observed due to a much weaker plasmonic coupling inside the thinner dielectric layers of this sample, as shown also in Figs. 3(c) and 3(d). The reflectance spectra show only one dip at $\lambda=500$ nm. At the same wavelength, due to the onset of the Au interband transitions, the absorptance reaches its maximum and remains more or less constant for $\lambda \leq 500$ nm. Concerning the transmittance properties, the metamaterial is characterized by a spectrum peaked at about 520 nm, i.e., where Re($\epsilon_{\parallel}$)$\simeq 1$, indicating a matching of the refractive index between air and the metamaterial [13].

Moreover, the transmittance results approximately one third of that of MM16 in the whole spectrum due to the larger metal filling fraction. By varying the angle of incidence and the light polarization, the following effects are observed (similar to MM16): (i) the reflectance grows with the angle in TE configuration, whereas it diminishes by increasing the angle with TM-polarized light; (ii) the transmittance significantly reduces by increasing the angle in TE configuration (a blueshift of the peak of 10 nm is registered at TE 60°), whereas it remains approximately the same by varying the angle in TM configuration; (iii) the absorptance decreases with increasing angle for TE polarization while it increases with the angle for TM polarization. Finally, it is worthwhile to note that,

differently from the MM16 sample, the linear optical properties of MM33 are very similar to those of an Au thin film of thickness 60 nm (corresponding to the total thickness of the metallic layers in the sample, see Fig. S3 of the Supplemental Material [21]). In this case, the spectral response is strongly dominated by the losses triggered by the imaginary component of the Au dielectric permittivity [28,30].

B. Nonlinear optical properties

The nonlinear optical response of the produced metamaterials is spectrally investigated in a broad region around their λ_{ENZ} by the z-scan technique [31]. The measurements are performed as a function of the incidence angle with TE- and TM-polarized light.

As an example, in Figs. 4(a) and 4(b) we report the open-aperture (OA) and closed-aperture (CA) z-scan curves measured at normal incidence for MM16 (red) and MM33 (blue) at the corresponding ENZ wavelength ($\lambda_{\text{ENZ}} = 666$ nm and $\lambda_{\text{ENZ}} = 543$ nm). At the considered wavelengths both samples exhibit reverse saturable absorption (RSA, $\beta > 0$) and self-focusing (SF, $n_2 > 0$). In fact, the OA curves [Fig. 4(a)] show a valley in the transmittance trend at the focal point ($z = 0$), which is the portrayal of a RSA character. Instead, in the CA curve [Fig. 4(b)] SF is indicated by the typical valley-peak feature, i.e., the transmittance decreases in the prefocal region and shows a peak after the focus. In this case, the curves result asymmetric compared to the case of pure nonlinear refraction [31] because of the simultaneous existence of strong RSA and SF. The nonlinear parameters extracted from the analysis of the z scans for the sample MM16 result $\beta = 3.9 \times 10^{-5}$ cm/W and $n_2 = 2.7 \times 10^{-10}$ cm^2/W. For the MM33 sample, the valley in the OA curve results about 10% deeper than that of MM16, indicating a stronger nonlinear absorption, and a slight broadening can be noticed. Moreover, it is worth noting that in this case, in order to properly fit the OA scans, it is no longer possible to consider the nonlinear absorption coefficient as a constant, intensity-independent value (keeping at the same time the beam parameters, as the Rayleigh range, fixed in the fit) as in the standard z-scan analysis [31]. Instead, an intensity-dependent expression $\beta_S(I)$ as in Eq. (1) has to be considered, as explained in Ref. [32]:

$$\beta_S(I) = \frac{\beta}{1 + I/I_S}, \qquad (1)$$

where β has to be interpreted as the unsaturated nonlinear absorption coefficient of the metamaterial and I_S is the corresponding saturation intensity. From the scans in Fig. 4 (blue solid lines) for MM33 at $\lambda = 543$ nm we get $\beta = 3.7 \times 10^{-4}$ cm/W with $I_S = 435$ MW/cm^2, and $n_2 = 1.1 \times 10^{-9}$ cm^2/W; the light-blue dashed curves represent the best fits of the scans of MM33 that can be
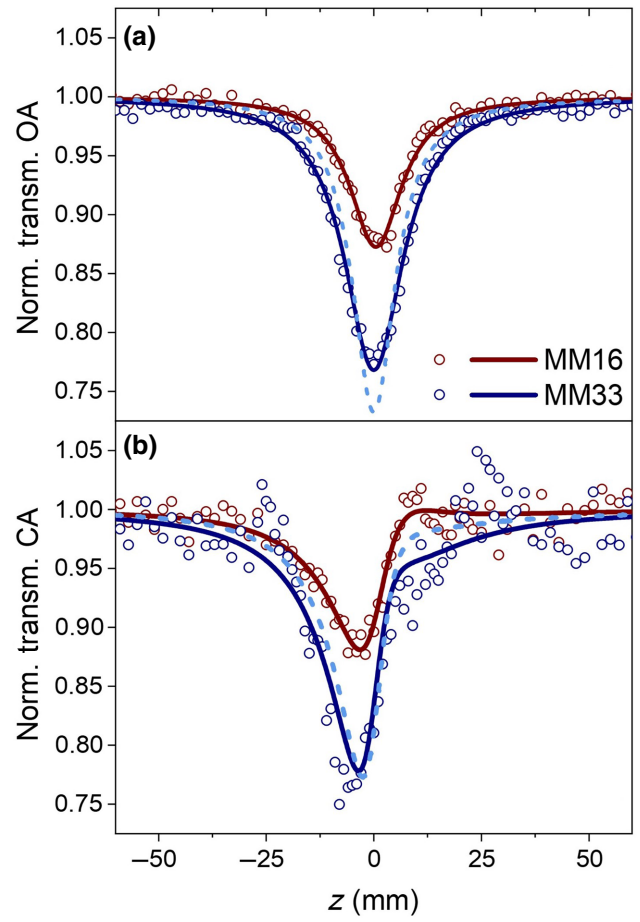

FIG. 4. Normalized OA (a) and CA (b) transmittance of MM16 (red) at $\lambda_{\text{ENZ}} = 666$ nm and MM33 (blue) at $\lambda_{\text{ENZ}} = 543$ nm. Both scans are performed at normal incidence. The open circles are the experimental data, whereas the solid lines are the best-fitting curves. The light-blue dashed lines are the best fits of the scans of sample MM33, obtained without considering the saturation effect of the nonlinear absorption coefficient. For sample MM16, no saturation has to be included to fit the scans.

obtained without considering the saturation effect. These results show that when comparing the nonlinear response at the ENZ wavelength of each sample, both β and n_2 of MM33 are larger than those of MM16 by approximately one order of magnitude. This is very likely due to the fact that in MM33, λ_{ENZ} falls closer to the region of the interband transitions of Au (around 500 nm), which give the dominant contribution to the nonlinear response, very likely as a consequence of the generation of hot electrons (Fermi smearing) [33–35].

The spectral nonlinear optical response as a function of the incidence angle and light polarization (TE and TM) for MM16 is displayed in Fig. 5. Panels (a)–(c) show the trends of β and n_2 in the entire explored spectral region (400–800 nm), while on the right of each panel an
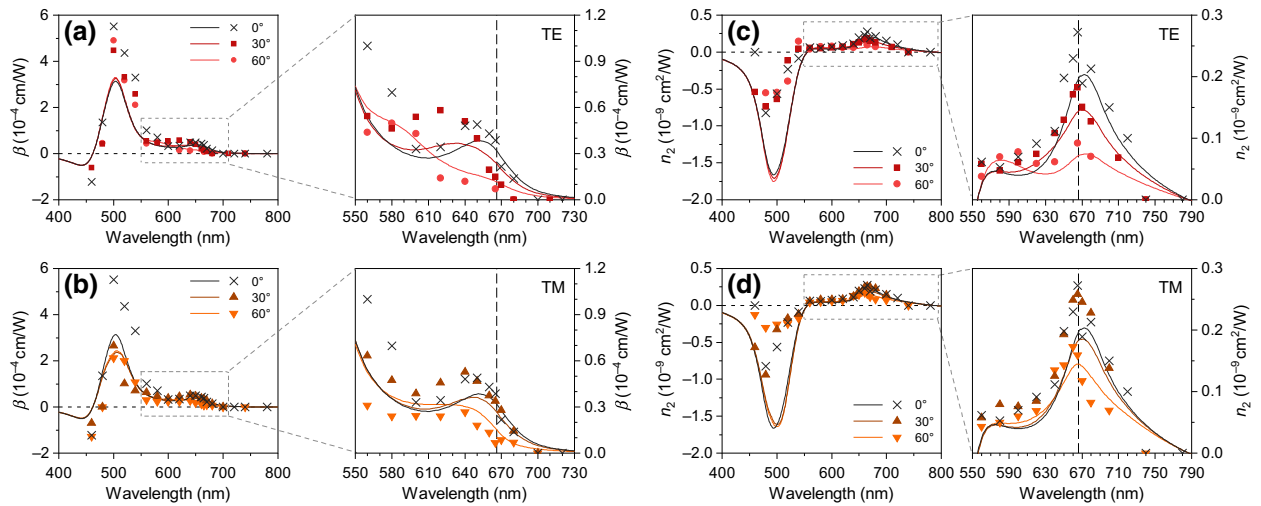
FIG. 5. (a),(b) Nonlinear absorption coefficient β and (c),(d) nonlinear refractive index n_2 of sample MM16 as a function of the wavelength. The measurements are performed at different incidence angles ($0°$, $30°$, $60°$) for TE (a),(c) and TM (b),(d) polarization. On the right of each panel an enlarged view of the trend around the λ_{ENZ} (vertical dashed line) of the sample is plotted. The error bars are of the order of 15% for each experimental point and are not depicted to improve data visualization. The solid lines are the results of simulations performed with the model described in the text.

enlarged view in the spectral region around the λ_{ENZ} (vertical dashed line) of the sample is reported. In Fig. S4 of the Supplemental Material [21] we report, as an example, a set of scans (OA and CA) taken at different wavelengths, angles of incidence and light polarization, with the corresponding fits from which the values in Fig. 5 are calculated. Across the explored range MM16 exhibits a RSA behavior ($\beta > 0$) with every configuration, with a peak of β at 500 nm. A negative value of β, characteristic of saturable absorbtion (SA) is measured at $\lambda = 480$ nm only. Moreover, at wavelengths shorter than 560 nm, namely in the spectral region corresponding to the onset of the interband transitions of gold, the nonlinear absorption response of the sample is characterized by a clear saturation effect and the intensity-dependent expression reported in Eq. (1) has to be used to fit the data (a saturation intensity of about $I_S \cong$ 0.2 GW/cm^2) is determined in this wavelength range). In Figs. 5(a) and 5(b) we report the values of the unsaturated nonlinear absorption coefficient β. Instead, at wavelengths longer than 580 nm no saturation effect is observed. By comparing the results obtained with the different configurations (angle of incidence and light polarization), it emerges that the nonlinear absorption coefficient of the sample follows a similar trend as its linear absorptance A (Fig. 2, bottom row, left panels). This is particularly evident in the wavelength range across the λ_{ENZ} of the sample [enlarged views in Figs. 5(a) and 5(b)]. At normal incidence, β shows a peak at 650 nm, located at the same λ of the absorptance peak, only 16 nm far from λ_{ENZ}; such peak damps and blueshifts by increasing the angle of incidence, with much larger variations in TE configuration. Regarding the nonlinear refraction properties, in all the

configurations a negative nonlinear refractive index, characteristic of self-defocusing (SD, $n_2 < 0$), is measured at wavelengths shorter than about 540 nm [Figs. 5(c) and 5(d)], while for longer wavelengths we observe the transition to SF ($n_2 > 0$). More interestingly, by looking closer at the ENZ region [enlarged views in Figs. 5(c) and 5(d)], a peak emerges at λ_{ENZ}, whose amplitude can be modulated by varying the incidence angle and the polarization of the light. Besides, it is worthwhile to notice that the peak in the nonlinear refractive index is slightly redshifted compared to the linear and nonlinear absorption peaks. As a consequence to this, in its hyperbolic regime (i.e., at $\lambda > \lambda_{ENZ}$) the metamaterial keeps non-null values of nonlinear refraction while both β and A rapidly drop, completely vanishing at $\lambda \geq 700$ nm. This last property may be highly relevant for the implementation of these metamateriels in all-optical switching devices, in which high nonlinear refraction coefficients with minimum linear and nonlinear absorption are required [36].

The spectral trend of β and n_2 measured for sample MM33 is reported in Fig. 6. OA and CA scans taken at different wavelengths, angles of incidence, and light polarization, with the corresponding fits, are shown in Fig. S5 of the Supplemental Material [21]. Similarly to MM16, for all the configurations the sample behaves as a reverse saturable absorber ($\beta > 0$) in the whole explored spectral range, with a peak of β at 500 nm, and a saturation effect is observed in the range 440–560 nm. Here Eq. (1) is employed to fit the measured OA scans; the resulting saturation intensity values are of the order of $I_S \cong$ 0.4 GW/cm^2. However, in this case a much stronger nonlinear absorption (about a factor 2.5 larger than MM16)

is measured between 440 and 560 nm, whereas at longer wavelengths β tends to vanish. In both TE and TM configurations the trend of β is not considerably modified by increasing the angle of incidence, but we observe a progressive decrease of its value. Regarding the nonlinear refractive index [Figs. 6(c) and 6(d)], as for MM16, the sample exhibits a sign inversion at about 520 nm, changing its response from self-defocusing ($n_2 < 0$) to self-focusing ($n_2 > 0$), and the maximum n_2 is measured at wavelengths around $\lambda_{\text{ENZ}} = 543$ nm, with a monotonic decrease to zero for longer wavelengths. Moreover, the spectral trend of n_2 remains the same at all the considered angles of incidence. The obtained results show that the nonlinear optical response of MM33 is dominated by the metallic component, as observed for the linear optical properties. To highlight this, in Fig. S6 of the Supplemental Material [21] we report the spectral characterization of the nonlinear absorption coefficient and the nonlinear refractive index of a gold thin film deposited on a soda-lime glass substrate. The measurements are taken both for a film of 15 nm thickness (corresponding to that of a single Au layer in the multilayers) and for a film of 60 nm (i.e., the total thickness of the metallic layers): no differences are observed and the data can be fitted as a single set, thus proving that the measured response represents the intrinsic nonlinear response of the metallic component. Consistently, no difference by varying the angle of incidence or the light polarization is observed in the Au thin films. The trends of the nonlinear optical parameters are in agreement with the results reported in the literature for Au thin films [9,33]. Nonetheless, it is worthwhile to stress that the nonlinear optical response of metals strongly depends on the experimental conditions used for the measurements (beam pulse duration, repetition rate, beam peak intensity etc...) [33,37], so possible quantitative differences can be due to different measurement parameters. By comparing the results for the sample MM33 (in Fig. 6) with the data of the Au thin films (Fig. S6 of the Supplemental Material [21]), it is evident that at normal incidence the MM33 sample behaves as the Au thin film, both in terms of the spectral trend and from the quantitative point of view. However, the modulation of the nonlinear optical properties can be obtained in the multilayer by tilting the sample or changing the light polarization. On the other hand, looking back at the results for MM16 (Fig. 5), its nonlinear parameters emerge to have the same trend as the metallic component at wavelengths shorter than 560 nm, i.e., in the spectral region corresponding to the Au interband transitions, even though the response is damped likely as a consequence of the smaller metallic filling fraction in this sample. Nonetheless, differently from MM33 and the Au thin films, in MM16 at wavelengths longer than 560 nm we observe a nonlinear response, which is peaked around its ENZ wavelength ($\lambda_{\text{ENZ}} = 666$ nm) and is strongly tunable by selecting the angle of incidence or the light polarization. In order to

simulate the nonlinear optical response of the samples in the different configurations (angle of incidence and light polarization), we apply the model described in Sec. IV to calculate the complex nonlinear refractive index of the metamaterials. In summary, the complex nonlinear refractive index of the metamaterials is calculated from Eq. (14), with the angle-dependent effective third-order susceptibilities given by expressions (19) and (24), respectively, for TE and TM polarization. Moreover an angle-dependent effective metal filling fraction [$\phi_m(\lambda, \theta)$, see Eq. (25)] is introduced in the expression for $\chi_{\text{TE}}^{(3)}(\theta)$ and $\chi_{\text{TM}}^{(3)}(\theta)$. Such an effective metal filling fraction allows us to account for the local intensity enhancement in the metamaterials and its angular dependence, as shown in Fig. 3, which is the dominant contribution to the angle-dependent nonlinear optical response observed in the metamaterials. In this way, for TE polarization we get

$$\tilde{n}_{2,\text{TE}}(\theta) = \frac{3}{4c\epsilon_0\tilde{n}_0 n_0}\chi_{\text{TE}}^{(3)}(\theta) = \frac{\tilde{n}_m n_m}{\tilde{n}_0 n_0}\tilde{n}_{2,m}\phi_m^{\text{TE}}(\theta), \quad (2)$$

while for TM polarization it results

$$\begin{aligned}\tilde{n}_{2,\text{TM}}(\theta) &= \frac{3}{4c\epsilon_0\tilde{n}_0(\theta)n_0(\theta)}\chi_{\text{TM}}^{(3)}(\theta) \\ &= \frac{\tilde{n}_0(\theta)\tilde{n}_m n_m}{n_0(\theta)}\tilde{n}_{2,m}\phi_m^{\text{TM}}(\theta) \\ &\times \left[\frac{1}{\epsilon_\parallel} + \frac{1}{\epsilon_\perp}\left|\frac{\epsilon_\perp}{\epsilon_m}\right|^2\left(\frac{\epsilon_\perp}{\epsilon_m}\right)^2\right], \quad (3)\end{aligned}$$

where we make explicit the angular dependence of the different parameters. In Eqs. (2) and (3), $\tilde{n}_0$ is the complex refractive index (n_0 its real part) of the metamaterials, which is calculated at each incidence angle and polarization from the corresponding angle-dependent complex effective permittivities given in Eqs. (12) and (13). Analogously, $\tilde{n}_m(n_m)$ is the complex (real) refractive index of the metal component, experimentally determined by spectroscopic ellipsometry measurements performed on the reference Au thin films. The term $\tilde{n}_{2,m}$ is the complex nonlinear refractive index of the gold layers, determined from the z-scan measurements of the reference samples (see Fig. S6 of the Supplemental Material [21]) by inverting Eqs. (15) and (16). Then, the nonlinear coefficients (n_2 and β) of the metamaterials for the different configurations are derived from Eqs. (2) and (3) applying relations (15) and (16). The solid curves in Figs. 5 and 6 are the results of the simulations performed with this model. A good agreement between measured and simulated data is obtained in the broad spectral range explored and for all the configurations. In particular, by comparing the results for sample MM16 (Fig. 5) we can see that the model predicts pretty well the enhancement of the nonlinear coefficients at the ENZ wavelength ($\lambda_{\text{ENZ}} = 666$ nm) as well
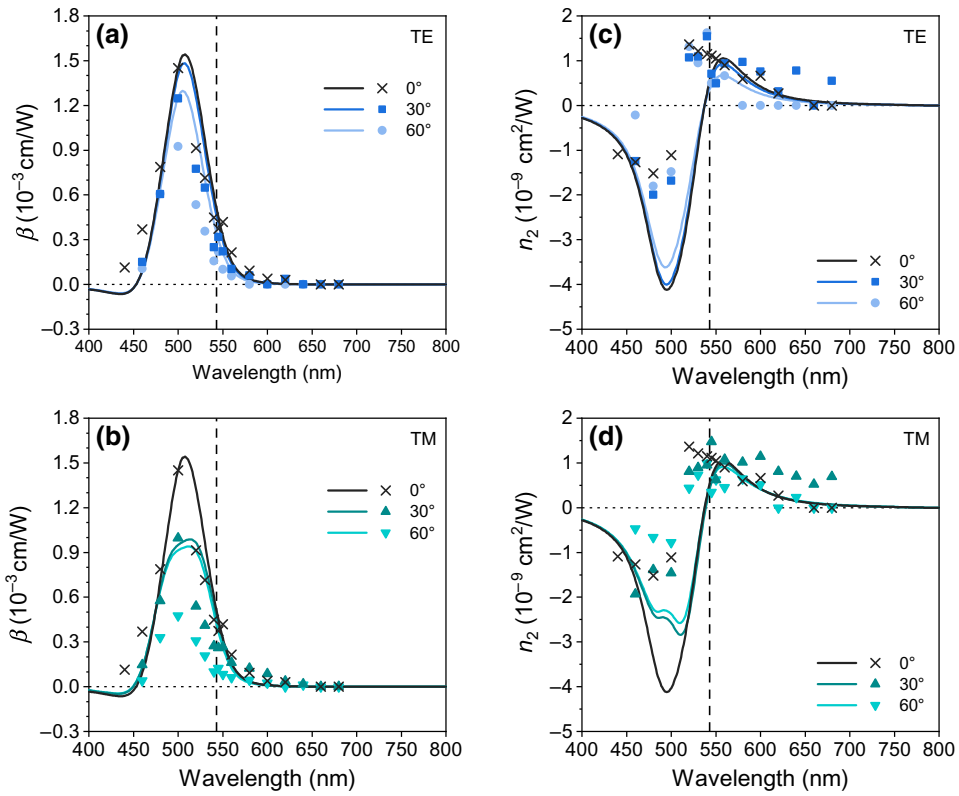
FIG. 6. (a),(b) Nonlinear absorption coefficient β and (c),(d) nonlinear refractive index n_2 of sample MM33 as a function of the wavelength. The measurements are performed at different incidence angles ($0°$, $30°$, $60°$) for TE (a),(c) and TM (b),(d) polarization. The error bars are of the order of 15% for each experimental point and are not depicted to improve data visualization. The solid lines are the results of simulations performed with the model described in the text.

as the observed spectral shift and damping when the sample is tilted with both TE and TM polarization. Such an enhancement of the nonlinear response at λ_{ENZ} is predicted by the model as a consequence of two concomitant effects occurring in the ENZ range: the linear permittivity becomes very small [$\mathrm{Re}(\epsilon_{\parallel}) \to 0$], and the effective metal filling fraction, $\phi_m(\lambda, \theta)$, has a peak. This last point is clearly highlighted in Fig. S7 of the Supplemental Material [21], where we report the maps, for TE and TM polarization, of the effective filling fraction calculated as a function of the wavelength and incidence angle; in Fig. S8 we plot the spectra of ϕ_m calculated for the two polarizations at the incidence angles considered in the experimental investigation. It is useful to point out that the angular dependence of the effective metal filling fraction ϕ_m introduced in Eqs. (2) and (3) is the dominant contribution with both polarization states and also explains the angular trend observed for TE polarization, where instead all the other parameters are angle independent. To better highlight this, as a comparison we report in Figs. S11 and S12 of the Supplemental Material [21] the results of the fits performed for the two metamaterials considering, instead of $\phi_m(\lambda, \theta)$, the geometrical filling fraction f_m, as done in Ref. [20]: the plots clearly show that this approach does not allow

us to reproduce well the measured spectral trend of the nonlinear parameters and it cannot describe the observed angular dependence, particularly for TE polarization. This further evidences that the local intensity enhancement, accounted for in the proposed model by the effective filling fraction $\phi_m(\lambda, \theta)$, is the driving force for the nonlinear optical response of this class of metamaterials. Moreover, for all the different configurations, the effective filling fraction exhibits an analogous trend as the linear absorptance of the samples (see Fig. 2), thus highlighting that in the considered metamaterials the intensity enhancement in the metallic layers plays a dominant role in controlling the linear absorption response of the samples, too.

Regarding sample MM33 (Fig. 6), the comparison between experimental and simulated data further confirms that the nonlinear response of this sample is dominated by that of the gold layers and therefore no enhancement is obtained at its ENZ wavelength ($\lambda_{\mathrm{ENZ}} = 543$ nm). However, it is worth stressing that on the whole the proposed model reproduces the observed spectral features rather well. The discrepancies in terms of absolute values can be attributed to possible deviations of the experimental samples from their nominal design as well as imperfections or defects in the constituent layers, which
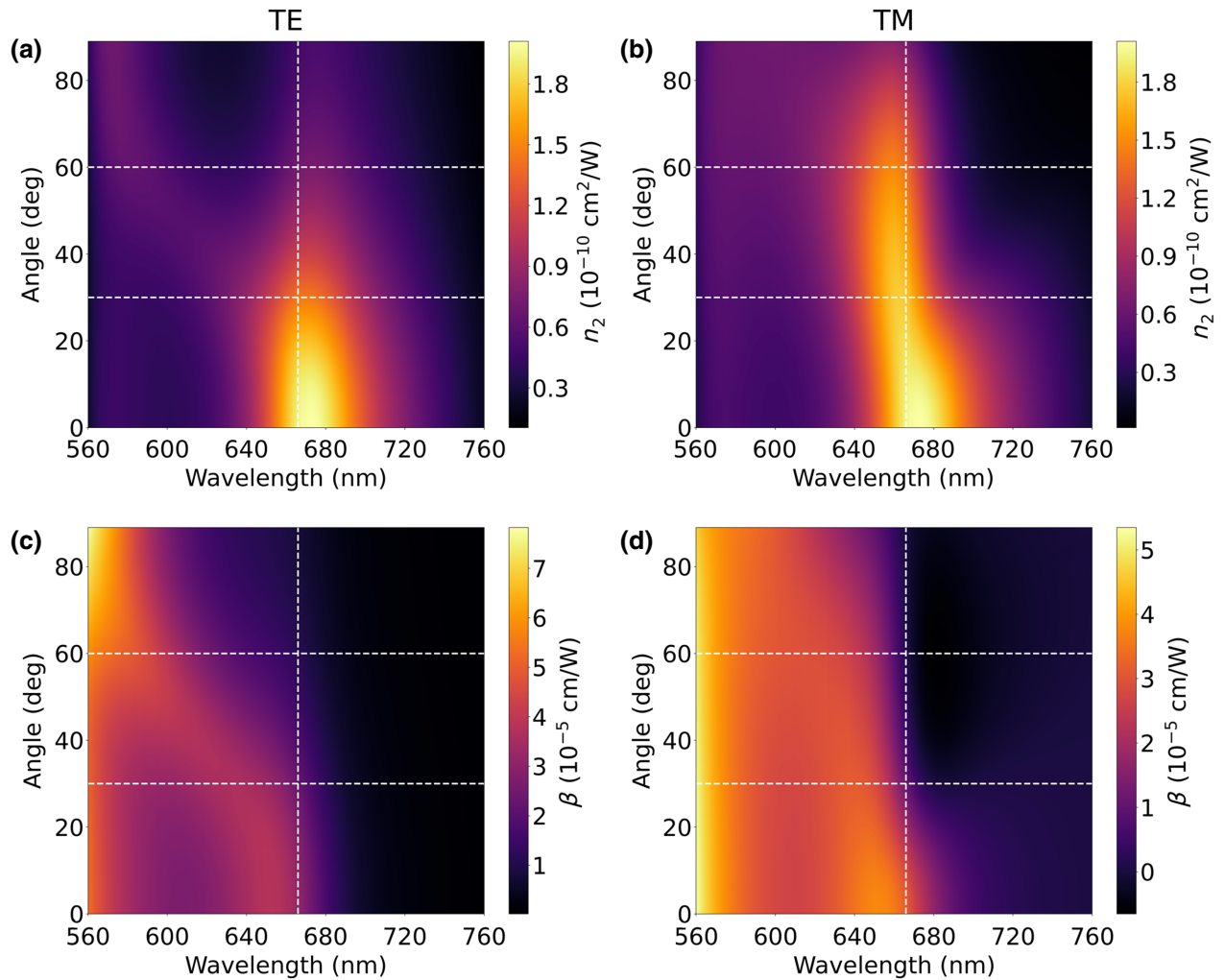
FIG. 7. (a),(b) Nonlinear refractive index n_2 and (c),(d) nonlinear absorption coefficient β of MM16 calculated in the ENZ region as a function of the incidence angle for TE (a),(c) and TM (b),(d) polarizations according to the proposed model. The vertical dashed lines indicate the ENZ wavelength while the horizontal dashed lines represent the angles considered for the experimental investigation.

can weigh especially in the region of the Au interband transitions. However, the overall agreement between the experimental results and the simulated ones is particularly significant considering the broad explored spectral range and the fact that no fitting parameters are introduced in the model.

To further corroborate the proposed model as a tool for the design of MM nonlinear optical properties, we calculate the nonlinear refractive index and the nonlinear absorption coefficient as a function of the incidence angle in the whole considered spectral range (see contour plots in Figs. S9 and S10 of the Supplemental Material [21]). In Fig. 7 we display the maps of n_2 and β, calculated as a function of the incidence angle in the ENZ spectral region for sample MM16. The contour plots clearly point out the formation of a peak of n_2 (a),(b) and β (c),(d) near λ_{ENZ} and its continuous variation with

the angle of incidence for TE (a),(c) and TM (c),(d) polarization. In particular, MM16 undergoes a gradual decrease of the nonlinear refractive index with increasing angle when impinged by TE-polarized light, whereas n_2 remains more stable even at higher angles of incidence for TM polarization. On the other hand, for TE polarization, the peak of β near λ_{ENZ} undergoes a remarkable shift towards shorter wavelengths with growing angle, thus gradually passing from being well separated from the peak generated by the metal-interband contribution to a condition for which they are totally joined above 60°. Differently, this blueshift is less pronounced with TM polarization, for which a wider band of positive β is formed between 560 and 670 nm, and a sign inversion can be also noticed at λ_{ENZ} over 30°. These features are well observed when λ_{ENZ} is well decoupled from the region of the metal-interband transitions, where instead

the nonlinear parameters assume higher absolute values and are quite invariable at different angles (see the full range contour plot in Fig. S9 of the Supplemental Material [21]). Beside this condition, the enhancement of the electric field at λ_{ENZ} in MM16, and thus its nonlinear response, is probably more favored than in MM33 also because of a lower (approximately half) imaginary part of the effective permittivity, thus making the field amplification in the ENZ region more significant. For the same reasons, the angular dependence of n_2 and β is almost unnoticeable in the contour plots of MM33, whose λ_{ENZ} is very close to the metal interband transitions region, where the metal absorption contribution drowns out that given by the ENZ field amplification (Fig. S10 of the Supplemental Material [21]).

III. CONCLUSION

The linear and third-order nonlinear optical properties of Au/Al$_2$O$_3$ multilayer metamaterials fabricated by magnetron sputtering depositions are spectrally investigated in a broad range in the visible spectrum at different incidence angles with TE- and TM-polarized light. Metamaterials with a different metallic filling fraction are produced by changing the thickness of the dielectric layers. In this way, the spectral position of the ENZ wavelength of the metamaterials is controlled, and thus the MM transition from elliptic to hyperbolic regime is spectrally tuned. The reported results demonstrate that the linear optical properties (reflectance, transmittance, and absorptance) and the nonlinear coefficients (nonlinear refractive index and nonlinear absorption coefficient) of the multilayer MMs can be varied by changing the metamaterial structure and a continuous modulation of the parameters can be obtained in a broad spectral range by tilting the samples, thus varying the incidence angle for both TE and TM polarization states. Moreover, a peak in the nonlinear response occurs at λ_{ENZ}, which is clearly highlighted when the ENZ wavelength of the metamaterials is well decoupled from the interband transitions region of the metallic component. The obtained results also suggest that the enhancement of the nonlinear optical properties is more favored when λ_{ENZ} falls in a wavelength region where the imaginary part of the effective permittivity approaches a null or very small value since the low loss allows a better exploitation of the field amplification due to the Re$\{\epsilon_\parallel\}$ zeroing. Finally, a model is proposed to simulate the nonlinear optical coefficients of the metamaterials taking into account their optical anisotropy: a good agreement between experimental and simulated results is obtained in the whole spectral range and for all the explored configurations without the introduction of any fitting parameter. In particular, the proposed model allows us to describe the experimentally observed angular dependence of the nonlinear parameters, which is demonstrated to be due to the angular dependence of

the electric field propagating inside the metamaterials, and it is accounted for in the model by an angle-dependent effective filling fraction. For this reason, this model represents a very useful tool to predict the third-order nonlinear optical response of multilayer metamaterials and its possible modulation by changing the experimental parameters (incidence angle and light polarization), and thus to design metamaterials with tailored nonlinear optical properties to be used for applications in different configurations.

IV. EXPERIMENTAL SECTION

A. Sample synthesis

Multilayer metamaterials are produced by magnetron sputtering depositions of Au and Al$_2$O$_3$ thin films on soda-lime glass substrates previously cleaned in an acidic piranha solution (H$_2$O$_2$:H$_2$SO$_4$ 1:3) at 80 °C for 1 h and rinsed with ultrapure Milli-Q water. The depositions are performed in argon inert atmosphere (working pressure $p = 5 \times 10^{-3}$ mbar) by means of a dc source for the gold target and a rf source for the alumina target. During the process, the sample holder is kept in rotation to ensure the homogeneity of the deposition. Two types of multilayer metal-dielectric MMs are synthesized by arranging Au and Al$_2$O$_3$ in a four-period structure with different metal filling fraction f_m. This is achieved by changing the thickness of the alumina layers (nominal thickness of 30 nm in one case and 80 nm in the other one), while the thickness of the gold layers is maintained equal to 15 nm (nominal value) for having the same metal absorption in each sample. In this way, the obtained MMs have $f_m = 33\%$ and $f_m = 16\%$, respectively. They are, respectively, named as MM33 and MM16, where the number represents the metal filling fraction. The same deposition conditions are used to obtain single thin films of gold (15 nm and 60 nm thickness) and alumina (30 nm and 85 nm thickness) as reference samples.

B. Morphological and linear optical characterization

The layered structure of the MMs is observed in cross-section by employing a Zeiss Sigma HD FE-SEM. Atomic force microscopy (AFM) measurements are made with a NT-MDT Solver Pro AFM to determine the surface roughness of the multilayer samples and the film thickness of the reference samples. The thickness of the layers in the MMs is accurately evaluated by fitting the results of variable-angle spectroscopic ellipsometry measurements of the MM samples with a multilayer input model. The measurements are performed by a J. A. Wollam V-VASE and the data analyzed by the WVASE software, obtaining $t_{Au} = 15.6$ nm and $t_{Al_2O_3} = 85.0$ nm for MM16, whereas $t_{Au} = 14.9$ nm and $t_{Al_2O_3} = 29.6$ nm for MM33, that are

compatible with the nominal thickness within their experimental margin of error (5%). Ellipsometric measurements are also made for the Au and Al_2O_3 reference samples to determine the dielectric permittivities of the constituent materials to be used for the numerical simulations. The results are reported in Fig. S13 of the Supplemental Material [21] and compared to tabulated functions [38,39]. The same ellipsometer is employed to obtain the reflectance and transmittance spectra of the produced MMs as a function of the incident angle and light polarization. The optical transmittance of the samples at normal incidence is measured by a UV-vis spectrophotometer (JASCO V670). All the ellipsometric measurements and the spectra are taken in the wavelength range 300–800 nm.

C. Numerical simulations

The electromagnetic linear response of the samples is simulated by EMUstack [26] on the basis of the scattering matrix method. The reflectance, transmittance, and absorptance spectra of the studied metamaterials are obtained as a function of the incidence angle by using the experimental optical functions of the constituent materials, extracted from the ellipsometric measurements performed on the reference films, as input parameters for the stack model taking into account the nominal geometrical features of the structure (i.e., the layer thickness).

D. z-scan measurements

The third-order nonlinear optical properties of the samples are spectrally studied by the z-scan technique [31]. A mode-locked Nd:YAG laser (Leopard, by Continuum) emitting pulses of 18 ps with a repetition rate of 10 Hz is used as the light source. The low repetition rate allows for heat dissipation between the pulses, preventing thermal accumulation effects [34]. The third harmonic ($\lambda =$ 355 nm) of the laser is employed to pump an optical parametric amplifier (TOPAS, by Light Conversion) that allows the spectral tuning of the laser beam in the 420–2400 nm wavelength range. The electric field of the laser beam at the exit of the optical parametric amplifier is vertically polarized. The output beam is spatially filtered to obtain a TEM_{00} Gaussian profile. Optical density (OD) filters are used to control the beam intensity. In the "z-scan line" the beam is focused by a 200-mm converging lens onto the sample, which is mounted on a motorized stage moving it along the lens focal axis (z direction). The sample is mounted vertically and the sample holder is rotatable around two axes, vertical and horizontal, so that TE and TM configurations are, respectively, obtained. The incident beam has a beam waist of $w_0 = 37.4$ μm at $\lambda = 600$ nm, measured by the knife-edge method [40]. OA and CA measurements are performed simultaneously thanks to a beam splitter that divides the light transmitted by the sample into two branches, collected by two Si

photodetectors. Along the CA branch an iris diaphragm with linear transmittance $S \simeq 0.3$ is positioned before the detector thus allowing sensitivity to phase distortions. A reference signal is also recorded by a third Si photodetector and it is used to compensate possible fluctuations of the incident laser-beam intensity. The signals of the three detectors are transduced by a digital oscilloscope (Tektronix TDS7104) and acquired by a computer using a home-made acquisition software. All the z scans are performed in the forward and backward direction to guarantee the absence of artifacts in the z-scan curves due to possible sample damage. Each point of the scans is acquired as the average of 150 laser shots. The measurements are performed with an average intensity of $I = 300$ MW/cm^2. In order to consider the real intensity penetrating the sample and activating the nonlinear response, taking into account the fraction lost by reflection, for each considered wavelength the beam intensity is calculated as $I = (1 - R)I_0$, where I_0 is the intensity of the input beam at the lens focus and R is the spectral reflectance of the sample (taken from the experimental data in Fig. 2). The nonlinear absorption coefficient β and nonlinear refractive index n_2 are, respectively, obtained from the open-aperture and closed-aperture normalized transmittance (T_{OA} and T_{CA}) curves for each considered wavelength [32,41,42]. For the CA scans, the normalized transmittance can be described by the following expression:

$$T_{CA} = 1 + \frac{(1 - S)^\mu \sin \xi}{S(1 + x^2)} \Delta\Phi_0 - \frac{1 - (1 - S)^\mu \cos \xi}{S(1 + x^2)} \Delta\Psi_0,$$

(4)

where

$$\mu = \frac{2(x^2 + 3)}{x^2 + 9},$$

(5)

$$\xi = -\frac{4x \ln(1 - S)}{x^2 + 9}.$$

(6)

S is the linear transmittance of the aperture and $x = z/z_0$ is the dimensionless relative position of the sample along the beam propagation path, with $z_0 = \pi w_0^2/\lambda$ being the beam Rayleigh range. For the case of OA scans, $S = 1$ and Eq. 4 becomes [31]

$$T_{OA} = 1 - \frac{\Delta\Psi_0}{1 + x^2}.$$

(7)

The OA and CA scans are independently analyzed by fixing the parameters obtained from the OA fit into the CA fit function in order to minimize the number of degrees of freedom and thus making the quantitative determination of the nonlinear parameters more reliable. From the fitting functions the nonlinear transmittance loss $\Delta\Psi_0$ and

the phase distortion $\Delta\Phi_0$ are extracted, to which β and n_2 are related according to [32]

$$\beta = \frac{2\sqrt{2}}{IL_e}\Delta\Psi_0, \qquad (8)$$

$$n_2 = \frac{\lambda}{2\pi IL_e}\Delta\Phi_0, \qquad (9)$$

where $L_e = [1 - \exp(-\alpha_0 L)]/\alpha_0$ is the sample effective length. The linear absorption coefficient is calculated as $\alpha_0 = (4\pi/\lambda)n_0\kappa$ [43], where n_0 and κ are the linear refractive index and extinction coefficient of the sample, whereas L is the sample thickness. In this way, Eqs. (8) and (9) take into account the real interaction length when the sample is tilted. n_0 and κ are calculated from the complex effective permittivity of the multilayer MMs [$\epsilon = (n_0 + i\kappa)^2$], taking into account the incidence angle and light polarization.

E. Linear effective permittivity of the multilayer metamaterials

In the limit of deep subwavelength thickness of the constituent layers, the *in-plane* ($\epsilon_\parallel = \epsilon_x = \epsilon_y$) and *out-of-plane* ($\epsilon_\perp = \epsilon_z$) complex effective permittivities of the multilayer MMs can be calculated according to the effective medium theory [22,23] using the following equation:

$$\epsilon_\parallel = f_m\epsilon_m + (1 - f_m)\epsilon_d, \qquad (10)$$

$$\epsilon_\perp = \frac{\epsilon_m\epsilon_d}{f_m\epsilon_d + (1 - f_m)\epsilon_m}, \qquad (11)$$

where f_m is the metal filling fraction, while ϵ_m and ϵ_d are the dielectric functions of the metallic and dielectric layers, respectively. ϵ_m and ϵ_d are experimentally measured by spectroscopic ellipsometry on the corresponding reference thin films.

For an input wave propagating within the metamaterial at an angle θ with respect to the normal to the layers' surface and linearly polarized in the plane of the surface (TE polarization), the complex effective permittivity of the metamaterial has no angular dependence and it is

$$\epsilon_{TE}(\theta) = \epsilon_\parallel \qquad (12)$$

Conversely for TM polarization it results

$$\epsilon_{TM}(\theta) = \frac{\epsilon_\parallel\epsilon_\perp}{\epsilon_\parallel\sin^2(\theta) + \epsilon_\perp\cos^2(\theta)}, \qquad (13)$$

where θ is the angle of propagation inside the metamaterial and it is related to the angle of incidence θ_i by Snell's law: $\sin(\theta_i) = \epsilon(\theta)\sin(\theta)$ [43].

F. Complex nonlinear refractive index ($\tilde{n}_2$) of the multilayer metamaterials

For a composite material, the complex nonlinear refractive index can be written in SI as [20,44]

$$\tilde{n}_2 = \frac{3}{4c\epsilon_0\tilde{n}_0 n_0}\chi_{eff}^{(3)}, \qquad (14)$$

where c is the speed of light in vacuum, ϵ_0 is the vacuum permittivity, $\tilde{n}_0$ the complex linear refractive index of the material (whose real part is n_0), and $\chi_{eff}^{(3)}$ is its third-order effective susceptibility. The nonlinear refractive index n_2 and the nonlinear absorption coefficient β are then related to Eq. (14) by the expressions:

$$n_2 = \text{Re}(\tilde{n}_2), \qquad (15)$$

$$\beta = \frac{4\pi}{\lambda}\text{Im}(\tilde{n}_2). \qquad (16)$$

For multilayer metamaterials such as those investigated in the present work, within a nonlinear effective medium theory, $\chi_{eff}^{(3)}$ can be written as a weighted average on the filling fractions of the third-order susceptibilities of the constituent materials, but different expressions are derived according to the polarization of the input electric field [45]. In particular, assuming that the third-order susceptibility of the dielectric component is much smaller than that of the metal ($\chi_d^{(3)} << \chi_m^{(3)}$) and can be neglected, the following expressions can be derived for the *in-plane* and *out-of plane* effective third-order susceptibility of the metamaterials, corresponding to the condition in which the input electric field is parallel to the surface of the layers or perpendicular to it [45]

$$\chi_\parallel^{(3)} = f_m\chi_m^{(3)}, \qquad (17)$$

$$\chi_\perp^{(3)} = f_m\chi_m^{(3)}\left|\frac{\epsilon_\perp}{\epsilon_m}\right|^2\left(\frac{\epsilon_\perp}{\epsilon_m}\right)^2, \qquad (18)$$

where $\epsilon_\perp$ is the *out-of-plane* complex effective dielectric permittivity of the metamaterials, given by Eq. (11), and ϵ_m is that of the metal. The ratio ($\epsilon_\perp/\epsilon_m$) represents the local-field enhancement factor for the metallic component [45].

For TE polarization, at all the angles of incidence it results

$$\chi_{TE}^{(3)}(\theta) = \chi_\parallel^{(3)}. \qquad (19)$$

In order to determine the angular dependence of the effective third-order susceptibility of the metamaterials for TM

polarization [$\chi_{\mathrm{TM}}^{(3)}(\theta)$], we consider the complex nonlinear effective permittivity for TM-polarized light given by the expression (in analogy with the angular-dependent linear permittivity given in Eq. 13) [9]:

$$\epsilon_{\mathrm{TM}}^{\mathrm{NL}}(\theta) = \frac{\epsilon_{\parallel}^{\mathrm{NL}}\epsilon_{\perp}^{\mathrm{NL}}}{\epsilon_{\parallel}^{\mathrm{NL}}\sin^2(\theta) + \epsilon_{\perp}^{\mathrm{NL}}\cos^2(\theta)}, \qquad (20)$$

where the *in-plane* ($\epsilon_{\parallel}^{\mathrm{NL}}$) and *out-of-plane* ($\epsilon_{\perp}^{\mathrm{NL}}$) nonlinear complex effective permittivities are [44]

$$\epsilon_{\parallel}^{\mathrm{NL}} = \epsilon_{\parallel} + \frac{3}{4}\chi_{\parallel}^{(3)}|E|^2, \qquad (21)$$

$$\epsilon_{\perp}^{\mathrm{NL}} = \epsilon_{\perp} + \frac{3}{4}\chi_{\perp}^{(3)}|E|^2. \qquad (22)$$

Replacing Eqs. (21) and (22) in Eq. (20), and assuming that the nonlinear terms in the denominator of Eq. (20) are negligible with respect to the linear terms, we get

$$\epsilon_{\mathrm{TM}}^{\mathrm{NL}}(\theta) \approx \epsilon_{\mathrm{TM}}(\theta) + \frac{3}{4}\epsilon_{\mathrm{TM}}(\theta)\left(\frac{\chi_{\parallel}^{(3)}}{\epsilon_{\parallel}} + \frac{\chi_{\perp}^{(3)}}{\epsilon_{\perp}}\right)|E|^2, \quad (23)$$

where we neglect the terms in order of $|E|^4$. Then, we get

$$\chi_{\mathrm{TM}}^{(3)}(\theta) = \epsilon_{\mathrm{TM}}(\theta)\left(\frac{\chi_{\parallel}^{(3)}}{\epsilon_{\parallel}} + \frac{\chi_{\perp}^{(3)}}{\epsilon_{\perp}}\right). \qquad (24)$$

From Eqs. (17) and (18), it emerges that both $\chi_{\parallel}^{(3)}$ and $\chi_{\perp}^{(3)}$ depend on the product $f_m\chi_m^{(3)}$. In the broad wavelength range explored, the third-order susceptibility of the metal (gold) has a strong dispersive character [33]. For this reason, considering also that nonlinear processes in metals can be differently activated according to the excitation conditions [33] and thus the nonlinear response may depend on the experimental conditions, in order to determine the third-order susceptibility of the gold layers we perform z-scan measurements on the reference samples (Au thin films of thickness 60 nm and 15 nm deposited on soda-lime glass substrates in the same conditions as for the metamaterials). The results are reported in Fig. S6 of the Supplemental Material [21]. The complex nonlinear refractive index of gold is then determined from Eqs. (15) and (16), from which, by inverting Eqs. (14), the spectral Au third-order susceptibility $\chi_{\mathrm{Au}}^{(3)}(\lambda)$ can be calculated. z-scan measurements in the whole explored spectral range are also performed on alumina reference samples (with thicknesses 30 and 85 nm). No nonlinear response is measured from these samples, thus confirming the hypothesis that the contribution due to the nonlinearity of the dielectric component can be neglected in the calculations.

On the other hand, the resonant behavior of the electric field distribution in the multilayers (see Fig. 3) has to be considered to provide a complete description of the nonlinear response of the MMs. This effect accounts for a local intensity enhancement in the metallic layers, which is demonstrated to be responsible for an enhanced nonlinear response in one-dimensional metal-dielectric photonic crystals [46,47]. Owing to this, a wavelength-dependent effective metal filling fraction can be defined as

$$\phi_m(\lambda, \theta) = f_m\frac{\zeta_{\mathrm{MM}}(\lambda, \theta)}{\zeta_{\mathrm{film}}(\lambda, \theta)}, \qquad (25)$$

where ζ_{MM} represents the spatial average of the square of the electric field over the metallic layers of the metamaterials while ζ_{film} is calculated for a gold thin film of 15 nm. The choice for considering a bulk Au film of 15 nm instead of 60 nm—i.e., the total thickness of the metallic layers in the metamaterials—is motivated by the exponential decrease of the electric field inside the Au film, so that the local intensity becomes too low to induce a nonlinear response in the film (for the 60-nm Au thin film, the local intensity decreases down to 50% in the first 15 nm). The calculations are done starting from the electric fields simulated by EMUstack. For the metamaterials, ζ_{MM} is calculated at all the incidence angles for the different incident polarizations (TE and TM). Figures S7 and S8 of the Supplemental Material [21] show the effective metal filling fraction of MM16 and MM33 calculated at the different incidence angles for TE and TM polarization. For MM16 the effective metal filling fraction ϕ_m is peaked close to the ENZ wavelength of the sample ($\lambda_{\mathrm{ENZ}} = 666$ nm, vertical dashed line), where it results almost double with respect to the volume fraction ($f_m = 0.16$, horizontal dashed line). This peak blueshifts and gets damped by increasing the incidence angle for both TE and TM polarization. Conversely, for MM33 the calculated effective metal filling fraction results smaller than the volume value ($f_m = 0.33$, horizontal dashed line) in the whole spectral range, but still peaked close to the ENZ wavelength of the sample ($\lambda_{\mathrm{ENZ}} = 543$ nm, vertical dashed line).

[1] N. I. Zheludev, The road ahead for metamaterials, Science **328**, 582 (2010).

[2] W. Cai and V. Shalaev, *Optical Metamaterials. Fundamentals and Applications* (Springer-Verlag, New York, USA, 2010), 1st ed.

[3] V. Shalaev, Optical negative-index metamaterials, Nat. Photonics **1**, 41 (2007).

[4] M. Kauranen and A. V. Zayats, Nonlinear plasmonics, Nat. Photonics **6**, 737 (2012).

[5] T. Pertsch and Y. Kivshar, Nonlinear optics with resonant metasurfaces, MRS Bulletin, 210 (2020).

[6] C. M. Soukoulis and M. Wegener, Past achievements and future challenges in the development of three-dimensional photonic metamaterials, Nat. Photonics **5**, 523 (2011).

[7] H. Husu, R. Siikanen, J. Mäkitalo, J. Lehtolahti, J. Laukkanen, M. Kuittinen, and M. Kauranen, Metamaterials with tailored nonlinear optical response, Nano Lett. **12**, 673 (2012).

[8] H. Sánchez-Esquivel, K. Y. Raygoza-Sanchez, R. Rangel-Rojo, B. Kalinic, N. Michieli, T. Cesca, and G. Mattei, Ultra-fast dynamics in the nonlinear optical response of silver nanoprism ordered arrays, Nanoscale **10**, 5182 (2018).

[9] A. D. Neira, N. Olivier, M. E. Nasir, W. Dickson, G. A. Wurtz, and A. V. Zayats, Eliminating material constraints for nonlinearity with plasmonic metamaterials, Nat. Commun. **6**, 1 (2015).

[10] A. V. Zayats, S. A. Maier, eds., *Active plasmonics and Tuneable Plasmonic Metamaterials* (John Wiley & Sons, Hoboken, New Jersey, USA, 2013).

[11] L. Kang, R. P. Jenkins, and D. H. Werner, Recent progress in active optical metasurfaces, Adv. Opt. Mater. **7**, 1801813 (2019).

[12] T. Cesca, E. Vianey García-Ramírez, H. Sánchez-Esquivel, N. Michieli, B. Kalinic, J. Manuel Gómez-Cervantes, R. Rangel-Rojo, J. Alejandro Reyes-Esqueda, and G. Mattei, Dichroic nonlinear absorption response of silver nanoprism arrays, RSC Adv. **7**, 17741 (2017).

[13] R. Maas, J. Parsons, N. Engheta, and A. Polman, Experimental realization of an epsilon-near-zero metamaterial at visible wavelengths, Nat. Photonics **7**, 907 (2013).

[14] Niu Xinxiang, Hu Xiaoyong, Chu Saisai, and Gong Qihuang, Epsilon-near-zero photonics: A new platform for integrated devices, Adv. Opt. Mater. **0**, 1701292 (2018).

[15] A. Poddubny, I. Iorsh, P. Belov, and Y. Kivshar, Hyperbolic metamaterials, Nat. Photonics **7**, 948 (2013).

[16] H. N. S. Krishnamoorthy, Z. Jacob, E. Narimanov, I. Kretzschmar, and V. M. Menon, Topological transitions in metamaterials, Science **336**, 205 (2012).

[17] A. A. Basharin, C. Mavidis, M. Kafesaki, E. N. Economou, and C. M. Soukoulis, Epsilon near zero based phenomena in metamaterials, Phys. Rev. B **87**, 155130 (2013).

[18] V. Caligiuri, M. Palei, M. Imran, L. Manna, and R. Krahne, Planar double-epsilon-Near-Zero cavities for spontaneous emission and purcell effect enhancement, ACS Photonics **5**, 2287 (2018).

[19] A. Alù, M. G. Silveirinha, A. Salandrino, and N. Engheta, Epsilon-near-zero metamaterials and electromagnetic sources: Tailoring the radiation phase pattern, Phys. Rev. B **75**, 155410 (2007).

[20] S. Suresh, O. Reshef, M. Z. Alam, J. Upham, M. Karimi, and R. W. Boyd, Enhanced nonlinear optical responses of layered epsilon-near-zero metamaterials at visible frequencies, ACS Photonics **8**, 125 (2021).

[21] See Supplemental Material at http://link.aps.org/supplemental/10.1103/PhysRevApplied.16.064020 for more details about the structural and linear optical properties of the samples and simulations of the nonlinear optical parameters.

[22] T. Tumkur, Y. Barnakov, S. T. Kee, M. A. Noginov, and V. Liberman, Permittivity evaluation of multilayered

[23] C. L. Cortes, W. Newman, S. Molesky, and Z. Jacob, Quantum nanophotonics using hyperbolic metamaterials, J. Opt. **14**, 063001 (2012).

[24] K. V. Sreekanth, A. D. Luca, and G. Strangi, Experimental demonstration of surface and bulk plasmon polaritons in hypergratings, Sci. Rep. **3**, 3291 (2013).

[25] L. Ferrari, C. Wu, D. Lepage, X. Zhang, and Z. Liu, Hyperbolic metamaterials and their applications, Prog. Quantum Electron. **40**, 1 (2015).

[26] B. C. Sturmberg, K. B. Dossou, F. J. Lawrence, C. G. Poulton, R. C. McPhedran, C. M. de Sterke, and L. C. Botten, EMUstack: An open source route to insightful electromagnetic computation via the bloch mode scattering matrix method, Comput. Phys. Commun. **202**, 276 (2016).

[27] I. Avrutsky, I. Salakhutdinov, J. Elser, and V. Podolskiy, Highly confined optical modes in nanoscale metal-dielectric multilayers, Phys. Rev. B **75**, 241402 (2007).

[28] S. Campione, F. Marquier, J.-P. Hugonin, A. R. Ellis, J. F. Klem, M. B. Sinclair, and T. S. Luk, Directional and monochromatic thermal emitter from epsilon-near-zero conditions in semiconductor hyperbolic metamaterials, Sci. Rep. **6**, 34746 (2016).

[29] V. Caligiuri, M. Palei, G. Biffi, S. Artyukhin, and R. Krahne, A semi-classical view on epsilon-near-Zero resonant tunneling modes in metal/Insulator/Metal nanocavities, Nano Lett. **19**, 3151 (2019).

[30] B. Harbecke, B. Heinz, and P. Grosse, Optical properties of thin films and the berreman effect, Appl. Phys. A **38**, 263 (1985).

[31] M. Sheik-Bahae, A. Said, T.-H. Wei, D. Hagan, and E. V. Stryland, Sensitive measurement of optical nonlinearities using a single beam, IEEE J. Quantum Electron. **26**, 760 (1990).

[32] T. Cesca, P. Calvelli, G. Battaglin, P. Mazzoldi, and G. Mattei, Local-field enhancement effect on the nonlinear optical response of gold-silver nanoplanets, Opt. Express **20**, 4537 (2012).

[33] R. W. Boyd, Z. Shi, and I. De Leon, The third-order nonlinear optical susceptibility of gold, Opt. Commun. **326**, 74 (2014).

[34] N. Rotenberg, A. D. Bristow, M. Pfeiffer, M. Betz, and H. M. van Driel, Nonlinear absorption in Au films: Role of thermal effects, Phys. Rev. B **75**, 155426 (2007).

[35] A. R. Rashed, B. C. Yildiz, S. R. Ayyagari, and H. Caglayan, Hot electron dynamics in ultrafast multilayer epsilon-near-zero metamaterials, Phys. Rev. B **101**, 165301 (2020).

[36] M. Samoc, K. Matczyszyn, M. Nyk, J. Olesiak-Banska, D. Wawrzynczyk, P. Hanczyc, J. Szeremeta, M. Wielgus, M. Gordel, L. Mazur, R. Kolkowski, B. Straszak, M. P. Cifuentes, and M. G. Humphrey, in *Organic Photonic Materials and Devices XIV*, edited by C. Tabor, F. Kajzar, T. Kaino, and Y. Koike (SPIE, 2012).

[37] H. Qian, Y. Xiao, and Z. Liu, Giant kerr response of ultrathin gold films from quantum size effect, Nat. Commun. **7**, 13153 (2016).

[38] P. B. Johnson and R. W. Christy, Optical constants of the noble metals, Phys. Rev. B **6**, 4370 (1972).

[39] I. H. Malitson, Refraction and dispersion of synthetic sapphire, JOSA **52**, 1377 (1962).

[40] J. M. Khosrofian and B. A. Garetz, Measurement of a gaussian laser beam diameter through the direct inversion of knife-edge data, Appl. Opt. **22**, 3406 (1983).

[41] S.-L. Guo, J. Yan, L. Xu, B. Gu, X.-Z. Fan, and N. B. Ming, Second z-scan in materials with nonlinear refraction and nonlinear absorption, J. Opt. A: Pure Appl. Opt. **4**, 504 (2002).

[42] D. Genchi, R. Rangel-Rojo, J. Bornacelli, A. Crespo-Sosa, A. Oliver, and T. Cesca, Spectral Nonlinear Optical Response of Ion-Implanted Au and Ag Nanoparticles in Sapphire: A Three-Level Model Description, Phys. Rev. Appl. **14**, 044020 (2020).

[43] M. Born and E. Wolf, *Principles of Optics: Electromagnetic Theory of Propagation, Interference and Diffraction of Light* (Cambridge University Press, Cambridge, UK, 1999), 7th ed.

[44] R. W. Boyd, *Nonlinear Optics* (Academic Press, San Diego, CA USA, 2008), 3rd ed.

[45] R. W. Boyd and J. E. Sipe, Nonlinear optical susceptibilities of layered composite materials, J. Opt. Soc. Am. B **11**, 297 (1994).

[46] N. N. Lepeshkin, A. Schweinsberg, G. Piredda, R. S. Bennink, and R. W. Boyd, Enhanced Nonlinear Optical Response of One-Dimensional Metal-Dielectric Photonic Crystals, Phys. Rev. Lett. **93**, 123902 (2004).

[47] R. S. Bennink, Y.-K. Yoon, R. W. Boyd, and J. E. Sipe, Accessing the optical nonlinearity of metals with metal–dielectric photonic bandgap structures, Opt. Lett. **24**, 1416 (1999).